Old Dominion University

ODU Digital Commons

2022

Solute Concentration Effects on Microstructure and the Compressive Strength of Ice-Templated Sintered Lithium Titanate

Rohan Parai
Old Dominion University

Ziyang Nie

Raina Hempley
Old Dominion University

Gary M. Koenig Jr.

Dipankar Ghosh
Old Dominion University

Follow this and additional works at: https://digitalcommons.odu.edu/mae_fac_pubs

Part of the Electro-Mechanical Systems Commons

Original Publication Citation

RESEARCH ARTICLE

Journal
American Ceramic Society

Solute concentration effects on microstructure and the compressive strength of ice-templated sintered lithium titanate

Rohan Parai[1] | **Ziyang Nie**[2] | **Raina Hempley**[1] | **Gary M. Koenig Jr.**[2] | **Dipankar Ghosh**[1] (ORCID)

[1]Department of Mechanical and Aerospace Engineering, Old Dominion University, Norfolk, Virginia, USA

[2]Department of Chemical Engineering, University of Virginia, Charlottesville, Virginia, USA

Correspondence
Dipankar Ghosh, Department of Mechanical and Aerospace Engineering, Old Dominion University, Norfolk, VA 23529, USA.
Email: dghosh@odu.edu

Abstract

This work investigated the role of sucrose and cationic dispersant (1-hexadecyl)trimethylammonium bromide concentration on ice-templated sintered lithium titanate microstructure and compressive strength, to enable a comprehensive understanding of composition selection and elucidate processing–microstructure–mechanical property relationships. Sucrose and dispersant concentrations were varied to change total solute concentration in suspensions and viscosity. Dispersant was more effective in reducing viscosity than sucrose; however, their combination had an even greater impact on reducing viscosity. Based on viscosity measurements, a total of 12 suspension compositions were developed, and materials were fabricated at two different freezing front velocity (FFV) regimes. Solute concentration greatly influenced ice-templated microstructure and microstructure development improved with solute concentration. Depending on solute concentration, type of solute, viscosity, and FFV, a wide variety of microstructures were observed ranging from lamellar to dendritic morphologies. Solute concentration effect was rationalized based on solid–liquid planar interface instability. For suspensions with comparable viscosity, solute concentration can be varied to tune microstructure, whereas for suspensions with comparable solute concentration, viscosity variation can tune microstructure. Compressive strength of sintered materials generally increased with total solute concentration, sucrose concentration, viscosity, and FFV. Due to the wide variety of microstructure, strength also varied over a wide range, 23–128 MPa.

KEYWORDS
compressive strength, ice-templating, lithium titanate, microstructure, solute concentration, viscosity

1 | INTRODUCTION

The ice-templating technique has gained attention to fabricate sintered electrode materials for lithium-ion batteries (LIBs).[1–4] This technique enables the synthesis of ceramic materials with directional, anisotropic pore channels, and the templated microstructure is tunable across multiple length scales.[5] Pore directionality and microstructure tunability in ice-templated materials have been suggested to be promising to improve the performance of LIBs.

Huang et al.[1] reported that ice-templated sintered lithium cobalt oxide (chemical composition $LiCoO_2$) cathode improved areal and gravimetric capacities in LIBs. Ice-templating was also applied to another oxide cathode material, $LiNi_{0.8}Co_{0.15}Al_{0.05}O_2$ (NCA), and a severalfold increase in area-specific capacity compared to conventional composite electrodes was observed.[2] Huang et al.[3] reported 67% higher energy density for LIBs with ice-templated thick lithium iron phosphate (LFP, chemical composition $LiFePO_4$) cathode compared to LIB with slurry cast LFP cathode. Ice-templated $LiFePO_4$/C composite electrodes exhibited a capacity retention of 93.3% even after 800 cycles at 1 C rate.[4] Zavareh et al.[6] showed that ice-templated LFP cathodes exhibited higher specific capacity and lower loss of energy density compared to conventional cathodes at 0.5 C rate. The authors have recently investigated electrochemical performance and compressive mechanical properties of ice-templated sintered lithium titanate oxide (LTO, chemical composition $Li_4Ti_5O_{12}$) anode materials.[7–10] The improved rate capability of ice-templated LTO anode was attributed to better Li-ion transport due to low pore tortuosity compared to conventional LTO anode.[7] The highest rate capability (increased retention of capacity with increasing rate of charge/discharge) in LIB was achieved when ice-templated sintered LTO anode was combined with a higher conductivity electrolyte.[8]

Although the recent developments in ice-templated sintered electrodes are promising, the fabrication landscape of these materials needs to be expanded. Mechanical properties of these electrodes are less explored, limiting the knowledge of structure–property relationships. Electrode strength is important for the performance of LIBs. Electrodes must withstand against external stresses that result from cell assembly, internal compression, which facilitates holding electrodes within the cell, and internal stresses that originate during electrochemical cycling.[11] Electrode failure due to these stresses will result in reduced accessible battery energy, power density and round trip efficiency, and decreased battery lifetime.[12]

Ice-templated microstructure and mechanical properties can be tuned by changing freezing front velocity (FFV, growth velocity of ice crystals),[13–15] additive type and concentration,[9,16] and particle size and shape.[14,15] Magnetic field,[17] ultrasound,[18] direct current electric field,[19] and alternating current electric field[20] have also been used to manipulate ice-templated microstructure. Additives are particularly very promising, which depress solvent freezing point, alter growth velocity and surface free energy of solvent crystals, and change viscosity, affecting crystal shape and thus pore size and morphology in the resulting ice-templated materials.

The impact of a number of additives on ice-templating processing and resulting microstructures of final materials has been explored previously. Glycerol addition has been shown to increase connectivity between ceramic walls and reduce pore size, where hydrogen bonds that form between water and glycerol limit ice crystal growth and decrease pore size.[21] The effect of *tert*-butyl alcohol on pore network characteristics has been studied.[22] Ethanol has shown to result in a bimodal pore width distribution.[16] Isopropyl alcohol resulted in elongated pores, reducing compressive strength.[23] Ethanol and 1-propanol have been shown to increase suspension viscosity, which inhibited the rejection of ceramic particles by ice crystals, increased resistance to crystal growth, and decreased wall spacing.[24] Compressive strength of the resulting materials improved due to increased connectivity among ceramic walls. Ammonium polyacrylate (NH_4PAA, anionic dispersant) has been used to reduce pore size.[25] Zirconium acetate (ZrAc) has been used to change pore morphology from lamellar to columnar.[26] Polyvinyl alcohol promotes the growth of secondary ice dendrites and thus reduces pore size and increases connectivity between walls, resulting in strength enhancement.[27,28] Thus, the general trend is that additives increase viscosity and limit the growth of solvent crystals, which reduce pore size and increase strength.

The authors recently showed that sucrose, a water-soluble additive less explored in ice-templating, can effectively tune the microstructure and compressive strength of ice-templated sintered LTO materials.[9,10] With the increasing sucrose concentration, templated morphology changed from lamellar to dendritic and compressive strength increased as high as eightfold. Parai et al.[10] also investigated the influence of sucrose concentration on microstructure in the transition and steady-state regions. The high water solubility of sucrose is beneficial for processibility. However, the previous studies were performed for high porosity (> 60 vol.%) sintered LTO materials. It is noted here that in our prior studies the target electrodes only contained electroactive materials free of binder and conductive additives, and this is also the target architecture of interest for the mechanical characterization herein. However, ice-templating can also be applied to composite battery electrode architectures. In any case, there is a

pressing need to extend the sucrose-based fabrication of ice-templated porous, thin films of only electroactive materials into a lower porosity regime (∼50 vol.% or lower), which is more suitable for LIBs.[29]

This work systematically investigated the role of the concentration of sucrose and a cationic dispersant on ice-templated microstructure and compressive strength. A series of aqueous LTO suspension compositions were developed but all with 27 vol.% LTO content. Sucrose and cationic dispersant concentrations were varied to change total solute concentration and viscosity. Materials were fabricated at two different FFV regimes. By making deliberate compositional changes and varying the unidirectional freezing conditions, a series of ice-templated LTO materials were developed to enable a comprehensive understanding of the composition selection in the sucrose-based fabrication of low porosity (∼50 vol.%) sintered electrodes and elucidate processing–microstructure–mechanical property relationships.

2 | EXPERIMENTAL PROCEDURES

2.1 | Preparation of aqueous LTO suspensions

NANOMYTE BE-10 LTO powder (purity > 98%) was purchased from NEI Corporation, Somerset, NJ. A two-step sieving process was used to break the agglomerates that were present in the as-received LTO powder; the details of the process can be found elsewhere.[9] All suspensions contained deionized (DI) water, 27 vol.% LTO powder, and sucrose (Saccharose, Sigma-Aldrich, Burlington, MA) of varying concentrations (C_{su}) between 1 and 6 wt.% (weight of sucrose with respect to DI water content in suspension). Sucrose also acted as a binder for green bodies. A cationic dispersant (1-hexadecyl)trimethylammonium bromide (CTAB, Alfa Aesar, Haverhill, MA) was used to change suspension viscosity and increase total solute concentration (C_s, mol/L). CTAB concentrations (C_{CT}) used were 0.02, 0.03, and 0.05 g/cm³ (weight of dispersant with respect to DI water volume in suspension). With respect to DI water content, 0.02, 0.03, and 0.05 g/cm³ CTAB corresponded to 2, 3, and 5 wt.% CTAB.

Sucrose was first dissolved in DI water, and then LTO powder was added. For suspensions with CTAB, dispersant was added before the addition of LTO powder. The addition of 0.03 and 0.05 g/cm³ CTAB caused foaming in suspensions, thus an anti-foaming agent (SURFYNOL 104 PG 50) was used for those suspensions, in the proportion of 0.1 wt.% of LTO powder. Suspensions were milled for 1 h at 30 RPM using zirconia (ZrO_2) spheres (5 mm diameter) with 1:4 mass ratio to LTO powder. Next, ZrO_2 spheres were

separated from suspensions using a 325-mesh sieve (45-μm openings). Viscosity (η) was measured using an Anton Paar MCR302 rheometer at room temperature. For each composition, three measurements were conducted to assess reproducibility. For a set of selected compositions, zeta potential (ζ), and particle size were measured using Zetasizer Nano-ZS90 (Malvern Panalytical, UK). Very dilute suspensions (0.0001g/cm³ LTO concentration) were used for analysis with the Zetasizer. A 12 mm × 12 mm × 45 mm cuvette was used for the test and ∼1ml suspension was added into the cuvette. For particle size measurement, the cuvette was loaded into the Zetasizer. For ζ measurement, a Zeta dip cell was inserted into the cuvette before the cuvette was put into the instrument. For each composition, average particle size and ζ were determined from at least 20 scans.

2.2 | Suspension compositions and fabrication of ice-templated sintered LTO materials

Table 1 lists the compositions and total solute concentration (C_s) of suspensions from which ice-templated materials were fabricated. Materials were fabricated from 1, 3, and 6wt.% sucrose-based suspensions. For each sucrose wt.%, materials were fabricated from four compositions: suspensions containing (i) LTO and sucrose; (ii) LTO, sucrose, and 0.02g/cm³ CTAB; (iii) LTO, sucrose, and 0.03g/cm³ CTAB; and (iv) LTO, sucrose, and 0.05g/cm³ CTAB. Thus, a total of 12 compositions and 4 samples were fabricated for each composition at 2 different FFV regimes, totaling 96 samples. The selection of sucrose concentration and CTAB concentration was based on the viscosity results and to systematically vary C_s, which are discussed in Section 3. Here, 1S series refers to 1S, 1S-0.02C, 1S-0.03C, and 1S-0.05C. Similarly, 3S series refers to 3S, 3S-0.02C, 3S-0.03C, and 3S-0.05C. Finally, 6S series refers to 6S, 6S-0.02C, 6S-0.03C, and 6S-0.05C.

In the custom-made ice-templating device,[30] a key component is a thin copper (Cu) plate ("Cold-finger") on which a Teflon tube (inner diameter 16 mm, height 25 mm, and wall thickness 5 mm) was placed and filled with an LTO suspension. The entire assembly was inserted inside liquid nitrogen (N_2) Dewar but placed above the liquid level. When the Cu plate temperature reached below 0°C due to the influence of liquid N_2, ice crystals nucleated at the bottom of the suspension in contact with the Cold-finger and preferentially grew upward and LTO particles accumulated between ice lamellae. Frozen samples contained alternate layers of ice crystals and LTO particles with both LTO and ice layers oriented parallel to the direction of the temperature gradient. For each composition, 1 and 20mm

TABLE 1 Composition of aqueous lithium titanate oxide (LTO) suspensions from which ice-templated materials were fabricated

| | Suspension composition (total solute concentration, C_s) | | | |
CTAB Sucrose	No CTAB (C_s, mol/L)	0.02 g/cm³/2 wt.% (C_s, mol/L)	0.03 g/cm³/3 wt.% (C_s, mol/L)	0.05 g/cm³/5 wt.% (C_s, mol/L)
1 wt.%	1S (0.02)	1S-0.02C (0.08)	1S-0.03C (0.11)	1S-0.05C (0.17)
3 wt.%	3S (0.09)	3S-0.02C (0.14)	3S-0.03C (0.17)	3S-0.05C (0.22)
6 wt.%	6S (0.18)	6S-0.02C (0.23)	6S-0.03C (0.26)	6S-0.05C (0.31)

Note: CTAB concentration is provided both in g/cm³ and wt.%.

Abbreviation: CTAB, cationic dispersant (1-hexadecyl)trimethylammonium bromide.

gaps between Cold-finger and liquid N_2 were used to fabricate materials at relatively high FFV (HFFV) and low FFV (LFFV). For each composition and freezing condition, four samples were fabricated. Frozen samples were freeze-dried (2.5 L, Labconco, Kansas City, MI) for 96 h at a pressure of 0.014mbar and temperature of −50°C. Freeze-dried samples were sintered at 950°C for 2 h in an air atmosphere inside a tube furnace (NBD, T-1700-60IT).

2.3 | Porosity measurements, microstructure characterization, and mechanical testing

Sintered samples were 13 mm in diameter and 8 mm in height. From each LTO cylinder, a 3mm thick disk specimen was extracted at a height of 2 mm from the bottom of the porous LTO cylinder. The density of each disk (ρ^*) was estimated from measurements of mass using an analytical balance and dimensions using a Vernier Caliper (GEARWRENCH, 3756 D). Relative density was estimated as $\rho_r = \rho^*/\rho_s$, with ρ_s bulk density of LTO (3.47 g/cm³),[9] and total porosity from $p_t = (1 − \rho_r) \times 100$.

Microstructure was characterized using a desktop scanning electron microscope (SEM, Phenom Pure, Thermo Fisher Scientific). Using an open-source imageprocessing software Fiji—ImageJ (NIH, USA), pore area distribution was determined from SEM images. For each composition and FFV regime, four SEM images from top image plane (5mm height from bottom) of two randomly selected LTO disks were used. SEM images were segmented into ceramic and pore regions using "Trainable Weka Segmentation" plugin available in Fiji—ImageJ.

The uniaxial compressive mechanical response of sintered LTO disks was characterized using a mechanical testing machine (MTS, ALLIANCE RF/300) at a displacement rate of 0.5 mm/min. Loading platen surfaces were lubricated with petroleum jelly to minimize friction between specimen and platen surfaces. For each composition and FFV regime, four disks were tested. Specimens were compressed along the growth direction of ice crystals.
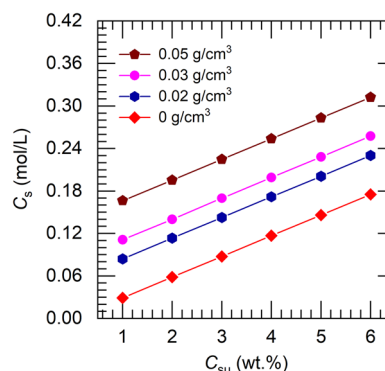

FIGURE 1 Variation of total solute concentration (C_s, mol/L) in aqueous lithium titanate oxide (LTO) suspensions with varying concentrations of sucrose (C_{su}, wt.%) and cationic dispersant (1-hexadecyl)trimethylammonium bromide (CTAB) (g/cm³)

3 | RESULTS AND DISCUSSION

3.1 | Dependence of viscosity and zeta potential on total solute concentration

Figure 1 shows the variation of C_s in LTO suspensions with varying C_{su} and C_{CT}. For suspensions with only sucrose, C_s increased from 0.02 mol/L for 1 wt.% sucrose to 0.18 mol/L for 6 wt.% sucrose. CTAB addition further increased C_s. For example, with 0.02g/cm³ CTAB, C_s of 0.18 mol/L can be achieved with 4wt.% sucrose. Figure 1 thus illustrates that C_s can be modified by systematically varying additive concentrations, and equivalent C_s can be achieved for various combinations of different additive concentrations. For identical C_s, η may vary depending on the proportions of sucrose and CTAB. Thus, by manipulating C_s and η using different proportions of the additives, ice-templated LTO microstructure, and mechanical properties can be tuned—the central focus of this work.

Figure 2 shows the variation of η with the shear rate of (A) LTO−sucrose, (B) LTO−CTAB, and (C) and LTO−sucrose−CTAB suspensions; all exhibited shear thinning behavior.[31] η values at shear rate 0.1 s⁻¹ are shown in for (D) LTO−sucrose, (E) LTO−CTAB, and (F) LTO−sucrose−CTAB suspensions. In LTO−sucrose suspensions, C_{su}
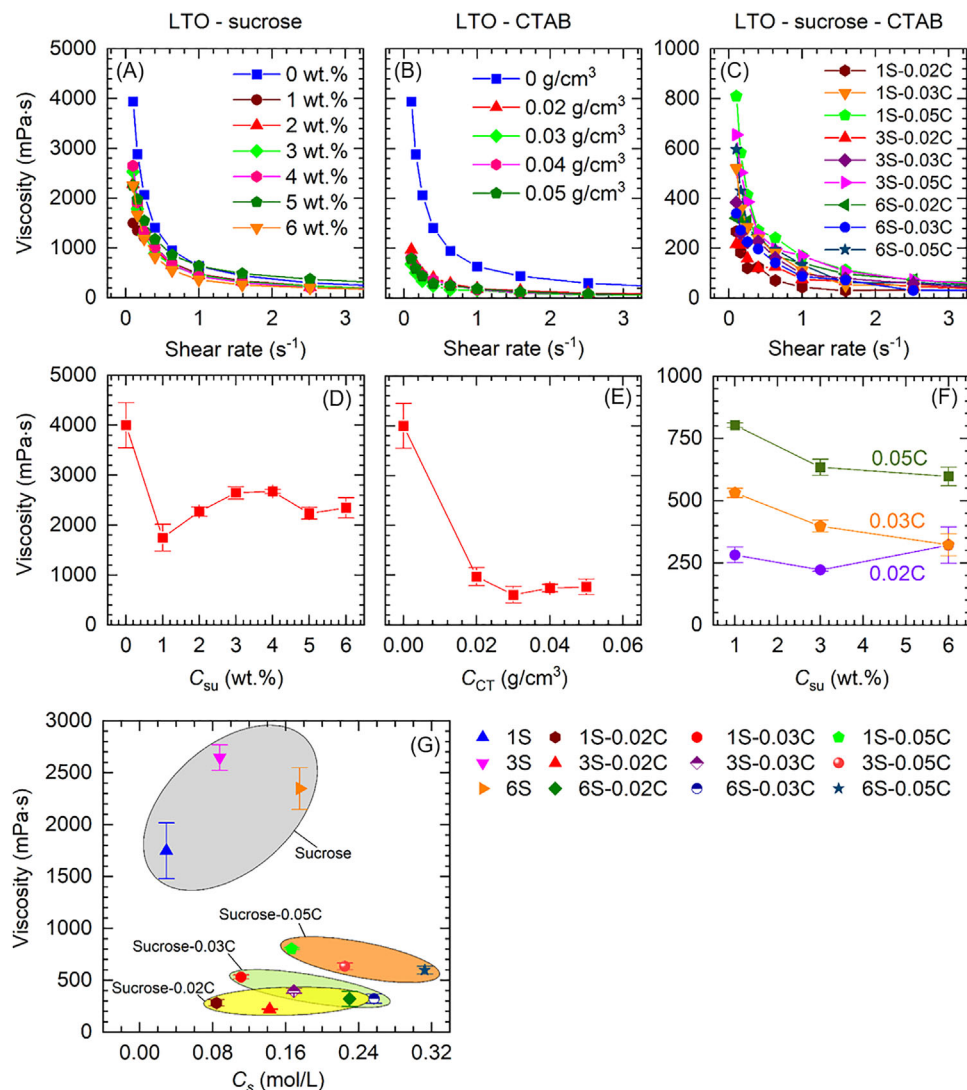
FIGURE 2 Variation of viscosity with shear rate for (A) lithium titanate oxide (LTO)–sucrose suspensions, (B) LTO–CTAB (cationic dispersant (1-hexadecyl)trimethylammonium bromide) suspensions, and (C) LTO–sucrose–CTAB suspensions. Viscosity values at shear rate of $0.1\ s^{-1}$ are shown in (D) for LTO–sucrose suspensions, (E) for LTO–CTAB suspensions, and (F) for LTO–sucrose–CTAB suspensions. (G) Variation of viscosity at shear rate of $0.1\ s^{-1}$ with total solute concentration (C_s) in selected LTO suspensions from which ice-templated materials were fabricated. Error in (D–F) represents the standard deviation for three individual viscosity measurements.

varied between 1 and 6 wt.%. In LTO–CTAB suspensions, C_{CT} varied between 0.02 and 0.05 g/cm³. In LTO–sucrose–CTAB suspensions, the concentration of both additives varied within the full range of the additives used in isolation.

The η of LTO–DI water suspension was 3998 ± 452 mPa·s. With the addition of only 1wt.% sucrose, η drastically reduced to 1749 ± 269 mPa·s, which may have been caused by the adsorption of sucrose molecules on the surface of LTO particles, resulting in steric repulsive forces among particles.[32–34] Above 1wt.% sucrose, η increased slightly, which could be due to the presence of excess sucrose molecules in water. Similar behavior has been reported in other studies.[10,33] CTAB had

a greater impact on η. For 0.02g/cm³ CTAB, η decreased to 973 ± 180 mPa·s compared to 3998 ± 452 mPa·s for LTO–DI water suspensions. ζ for LTO–DI water suspension was -22.8 ± 8.1 mV, suggesting negative surface charges on LTO particles. Therefore, positively charged CTAB molecules would be expected to adsorb on LTO surfaces, which may have caused electrosteric repulsions among particles and reduction in η.[35] Increase of C_{CT} did not really cause any further change with η consistently remained below 1000 mPa·s. Thus, CTAB was more effective in reducing η than sucrose. For LTO–sucrose–CTAB suspensions with 0.02g/cm³ CTAB, η decreased further to about 300 mPa·s at $0.1\ s^{-1}$. With the increasing C_{CT}, although η increased, but maximum
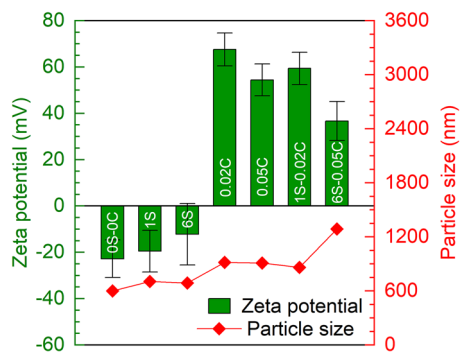
FIGURE 3 Zeta potential and particle size for different lithium titanate oxide (LTO) suspensions. Suspensions are labeled on the plot and from left to right were 0S-0C (LTO–DI water), 1S, 6S, 0.02C (LTO–DI water-0.02 g/cm³ cationic dispersant (1-hexadecyl)trimethylammonium bromide [CTAB]), 0.05C (LTO–DI water-0.05 g/cm³ CTAB), 1S-0.02C, 6S-0.05C. Error represents the standard deviation for 20 individual measurements.

η was about 800 mPa·s. Thus, compared to sucrose or CTAB alone, their combination had a greater impact on reducing η.

Figure 2G shows the relationship between η and C_s for selected LTO–sucrose and LTO–sucrose–CTAB suspensions used to fabricate ice-templated materials, which provides a rationale for composition selection in this study. For LTO–sucrose suspensions, η (>1500 mPa·s at 0.1 s⁻¹) was consistently higher than that of LTO–sucrose–CTAB suspensions (300–800 mPa·s at 0.1 s⁻¹). Figure 2G reveals that there are compositions with comparable C_s but distinctly different η, and with comparable η but different C_s. Thus, strategic selection of these suspensions enabled to study the influence of both η and C_s on ice-templated microstructure and strength.

Figure 3 shows ζ and LTO particle size for LTO–DI water (0S-0C), LTO–sucrose (1S, 6S), LTO–CTAB (0.02C, 0.05C), and LTO–sucrose–CTAB (1S-0.02C, 6S-0.05C) suspensions. The pH of these suspensions was close to 7, and the pH of DI water used to prepare the suspensions was 5.4. ζ was −22.8 ± 8.1 mV for LTO–DI water suspension, suggesting negative surface charges on LTO particles suspended in DI water. For 1S and 6S suspensions, ζ was −19.5 ± 9.01 and −12.2 ± 13.3 mV, respectively. The slight decrease could be due to the adsorption of sucrose molecules on the surfaces of LTO particles decreasing the particle surface charge. Overall, ζ values for DI water–LTO, 1S and 6S suspensions were in a comparable range. With the addition of sucrose, particle size increased from 600 to 700 nm, possibly due to the agglomeration of LTO particles, which could have been caused by reduced electrostatic repulsion between particles. As sucrose significantly reduced η

but ζ values were comparable for suspensions with and without sucrose, the reduction in η could be attributed to increased steric repulsion among LTO particles. Li et al.[36] suggested that in aqueous ceramic suspensions, one fraction of water molecules remains bound to particle surfaces referred to as bound water, whereas the other fraction of water molecules remains mobile that provides fluidity to suspension and is referred to as mobile (free) water. The presence of fructose (monosaccharide) reduced η of highly concentrated Al₂O₃ suspensions by reducing the fraction of water molecules bound to particle surfaces and thus increased the fraction of mobile water.[36] Similar behavior may also be expected for sucrose (a disaccharide made up of fructose and glucose monosaccharides).

For LTO–CTAB suspensions, 0.02 and 0.05g/cm³ CTAB drastically increased ζ to 67.6 ± 13.3 and 54.4 ± 7.1 mV, respectively. Positively charged CTAB molecules were adsorbed on the surfaces of LTO particles, resulting in a dramatic shift to a positive ζ. Adsorption of CTAB molecules on the surface of LTO particles creates a diffused layer around the particles,[35] which could be responsible for increased measured particle size in suspension (~900 nm). For 1S-0.02C suspension, ζ and particle size slightly changed to 59.4 ± 6.9 mV and 860 nm, respectively, whereas this suspension exhibited η (300 mPa·s) much lower than that of LTO–sucrose and LTO–CTAB suspensions. Although CTAB induced electrosteric repulsion among LTO particles, sucrose increased steric repulsion between particles and possibly increased the fraction of mobile water in suspensions. These mechanisms together in the presence of both sucrose and CTAB likely contributed to lowering η in LTO–sucrose–CTAB suspensions. For 6S-0.05C suspension, ζ significantly reduced to 36.7 ± 8.4 mV. Higher concentration of sucrose might have reduced charges on LTO particle surfaces and increased η. However, η (800 mPa·s) was still lower compared to LTO–sucrose and LTO–CTAB suspensions. Due to increased η, particle agglomeration increased, which resulted in a higher particle size of 1287 nm.

3.2 | Growth velocity of samples fabricated and porosity in sintered materials

Table 2 shows that materials were fabricated between 32–36 μm/s (relatively HFFV regime) and 21–25 μm/s (relatively LFFV regime). The porosity of all sintered LTO materials (Figure 4, Table 2) was between 47 and 52 vol.%. Thus, any potential variation in strength would be expected to be related to microstructure differences.

TABLE 2 Freezing front velocity (FFV) achieved in ice-templated lithium titanate oxide (LTO) materials fabricated at two selected gaps (between Cold-finger and liquid N_2) and porosity in corresponding sintered materials

Composition ID	Sucrose (wt.%)	CTAB (g/cm³)	1mm gap, high FFV		20mm gap, low FFV	
			FFV (μm/s)	Porosity (vol.%)	FFV (μm/s)	Porosity (vol.%)
1S	1	0	34.7 ± 0.9	48.3 ± 0.3	21.2 ± 0.6	48.8 ± 1.1
1S-0.02C	1	0.02	36.1 ± 1.2	50.6 ± 0.8	25.2 ± 1.5	49.6 ± 0.5
1S-0.03C	1	0.03	36.7 ± 1.1	47.8 ± 0.5	23.8 ± 0.3	50.4 ± 0.1
1S-0.05C	1	0.05	32.2 ± 2.0	48.6 ± 0.2	23.1 ± 1.4	49.2 ± 0.2
3S	3	0	32.7 ± 1.9	50.5 ± 0.3	22.1 ± 0.7	50.4 ± 0.7
3S-0.02C	3	0.02	36.2 ± 0.8	47.8 ± 0.5	23.6 ± 0.6	49.5 ± 0.1
3S-0.03C	3	0.03	33.5 ± 0.8	51.5 ± 0.1	23.5 ± 0.5	52.1 ± 0.1
3S-0.05C	3	0.05	36.8 ± 1.7	51.2 ± 0.2	24.6 ± 1.3	50.9 ± 0.2
6S	6	0	33.8 ± 1.5	51.1 ± 0.3	21.1 ± 0.9	49.4 ± 0.4
6S-0.02C	6	0.02	35.4 ± 1.2	47.8 ± 0.2	22.4 ± 0.3	49.5 ± 0.1
6S-0.03C	6	0.03	34.8 ± 1.2	50.4 ± 0.3	23.2 ± 0.5	50.7 ± 0.2
6S-0.05C	6	0.05	32.9 ± 1.5	50.3 ± 0.3	23.2 ± 0.3	49.7 ± 0.1

Note: Standard deviations represent errors for four independent samples.

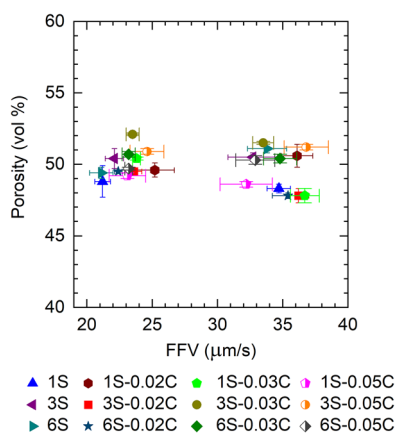Abbreviation: CTAB, cationic dispersant (1-hexadecyl)trimethylammonium bromide.

FIGURE 4 Porosity of ice-templated sintered lithium titanate oxide (LTO) materials of different compositions. Error represents the standard deviation for four independent disks.

3.3 | Ice-templated microstructure and processing–microstructure relationships

Figures 5–7 show SEM images of LTO materials, where image plane in each sample was located at 2mm (bottom plane) and 5mm (top plane) heights from the bottom of the sintered sample. In ice-templated ceramics, wall thickness and pore size increase along the sample height, that is, in the growth direction of ice crystals.[9,10,14] Thus SEM images revealed microstructure changes within 3mm height along the growth direction. Microstructure will be discussed in Sections 3.3.1–3.3.3, pore area distributions in Section 3.3.4, and processing–microstructure relationships in Section 3.3.5.

3.3.1 | Microstructure of 1S series materials

Figure 5 shows microstructures of sintered 1S series materials. Characteristic ice-templated microstructure was absent in 1S. With CTAB addition, templated microstructure developed, and microstructure development appears to improve with C_{CT}, that is, with C_s. With CTAB, morphology appears relatively dendritic at HFFV regime but lamellar in LFFV regime due to the reduced density of bridges. Increase in wall thickness and decrease in bridge density with a decrease in FFV, as well as along the growth direction are characteristics of ice-templated materials.[9,10,13–15] Ice-templated microstructure development was relatively poor in this series.

3.3.2 | Microstructure of 3S series materials

Figure 6 shows microstructures of sintered 3S series materials, which exhibited relatively well-developed microstructure. For all the materials, wall thickness increased with a decrease in FFV, as well as along sample height in both FFV regimes. However, at both FFV regimes, with the increasing C_{CT}, no clear trend emerged in wall thickness. In 3S series also, morphology was dendritic in HFFV regime but lamellar in LFFV regime. C_s in 3S (0.09 mol/L) was comparable to that in 1S-0.02C (0.08 mol/L), and the resultant materials from both compositions exhibited templated structure, attesting that the development of templated structure was dependent on C_s, which was sufficient in 3S suspensions. C_s in 3S-0.03C and that in 1S-0.05C suspensions were comparable; however,
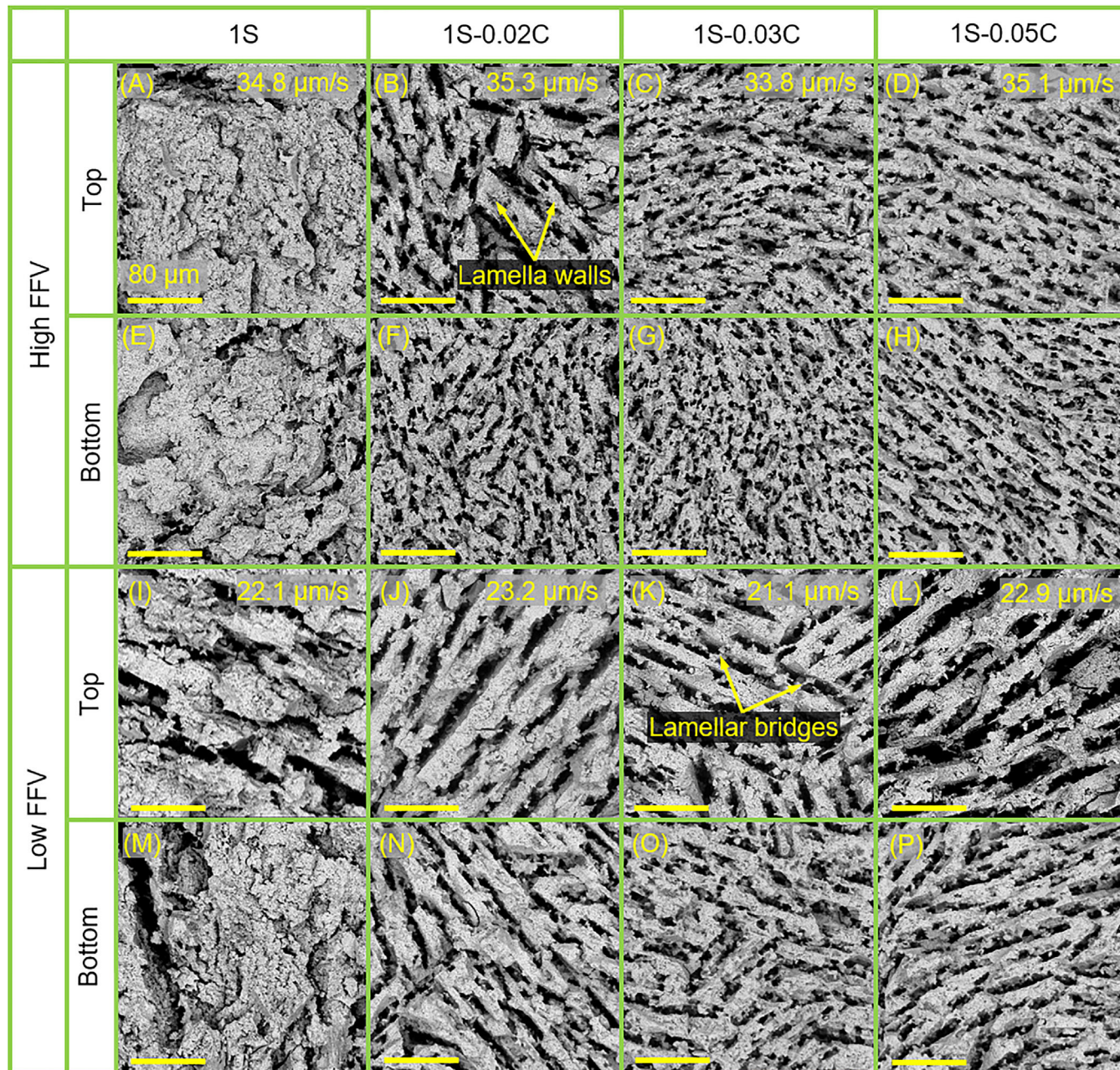
FIGURE 5 Representative scanning electron microscope (SEM) images from top (5mm height from bottom) and bottom (2mm height from bottom) image planes of sintered lithium titanate oxide (LTO) samples revealing microstructure of materials fabricated at high freezing front velocity (FFV) for compositions 1S (A and E), 1S-0.02C (B and F), 1S-0.03C (C and G), 1S-0.05C (D and H) and at low FFV for compositions 1S (I and M), 1S-0.02C (J and N), 1S-0.03C (K and O), 1S-0.05C (L and P)

the resultant microstructures were noticeably different, suggesting that comparable C_s would not necessarily result in similar ice-templated microstructure.

3.3.3 | Microstructure of 6S series materials

Figure 7 shows microstructures of sintered 6S series materials, which exhibited well-templated structure compared to 1S and 3S series. Microstructure in 6S series appeared dendritic at HFFV but lamellar at LFFV. With the increasing C_s and particularly at HFFV, microstructure appeared more dendritic. 6S and 1S-0.05C suspensions had comparable C_s, but distinctly different microstructures in the sintered materials. Similar observations were also made for 6S-0.02C and 3S-0.05C materials. Thus, the results again reinforce that comparable C_s would not necessarily result in similar ice-templated microstructure.
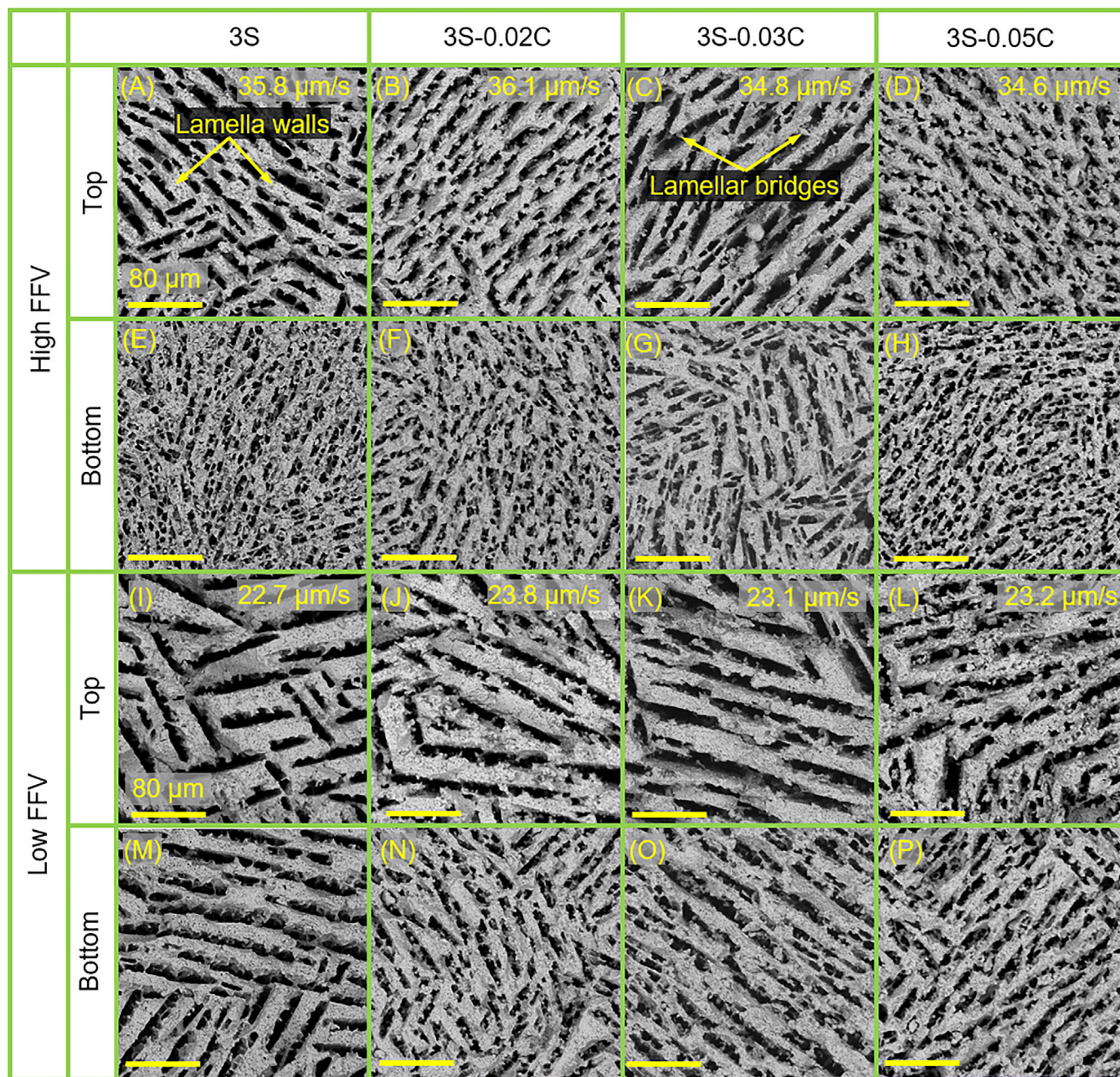
FIGURE 6 Representative scanning electron microscope (SEM) images from top (5mm height from bottom) and bottom (2mm height from bottom) image planes of sintered lithium titanate oxide (LTO) samples revealing microstructure of materials fabricated at high freezing front velocity (FFV) for compositions 3S (A and E), 3S-0.02C (B and F), 3S-0.03C (C and G), 3S-0.05C (D and H) and at low FFV for compositions 3S (I and M), 3S-0.02C (J and N), 3S-0.03C (K and O), 3S-0.05C (L and P)

In summarizing, C_s and FFV had a pronounced effect on ice-templated microstructure. Morphology in the materials was more generally dendritic at HFFV but lamellar at LFFV. SEM images suggested that bridge density increased with FFV. A significant conclusion was that templated microstructure development improved with C_s and dendritic feature in microstructure increased.

Microstructure changed considerably along the growth direction. For various compositions microstructure was dendritic on bottom image plane, particularly at HFFV but changed to lamellar by top image plane. It was thus difficult to ascertain a specific morphology. Qualitatively, 6S materials exhibited the best developed templated microstructure at both FFV regimes.
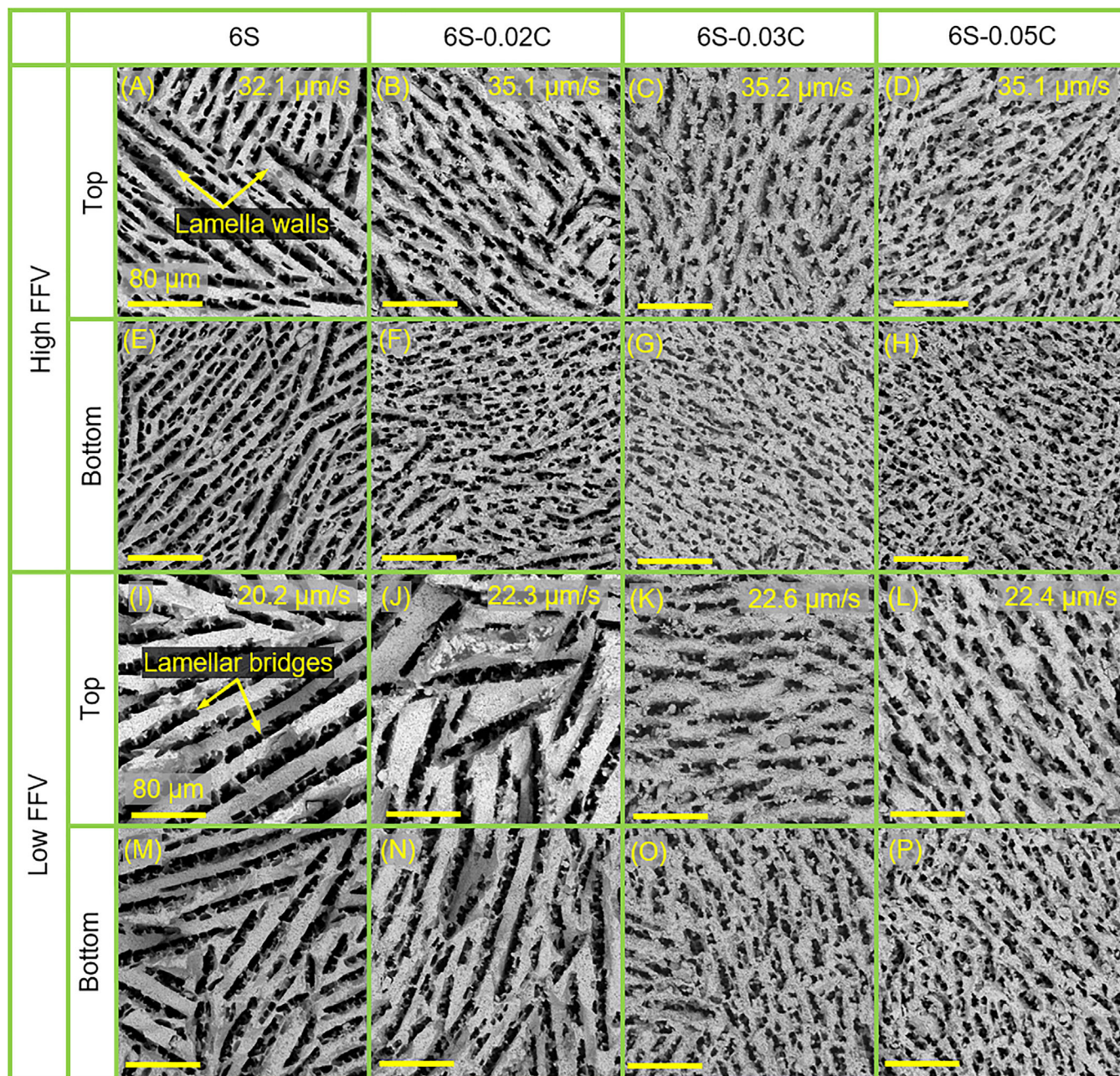
FIGURE 7 Representative scanning electron microscope (SEM) images from top (5-mm height from bottom) and bottom (2-mm height from bottom) image planes of sintered lithium titanate oxide (LTO) samples revealing microstructure of materials fabricated at high freezing front velocity (FFV) for compositions 6S (A and E), 6S-0.02C (B and F), 6S-0.03C (C and G), 6S-0.05C (D and H) and at low FFV for compositions 6S (I and M), 6S-0.02C (J and N), 6S-0.03C (K and O), 6S-0.05C (L and P)

3.3.4 | Quantitative microstructure analysis

Figure 8 shows the distribution of pore areas, representing the population of % pore area within each range (such as 0–50 μm^2) with respect to total pore area. For any composition, the general trend was that pore area distribution was narrow at HFFV but very broad at LFFV. HFFV materials contained a higher fraction of smaller pores than LFFV materials, which was expected as with the increasing

FFV, pore size decreases.[9,13–15] However, the trend was less straightforward with C_s. In HFFV 1S series, some increase occurred in the population of smaller pores with increasing C_s. A similar trend was also observed for HFFV 3S series, except for 3S-0.03C-HFFV. However, the trend was most prominent in HFFV 6S series. No clear trend emerged with C_s in LFFV regime, although in any series, materials with 0.05g/cm³ CTAB exhibited a relatively higher population of small pores. A caution needs to be made as the total area
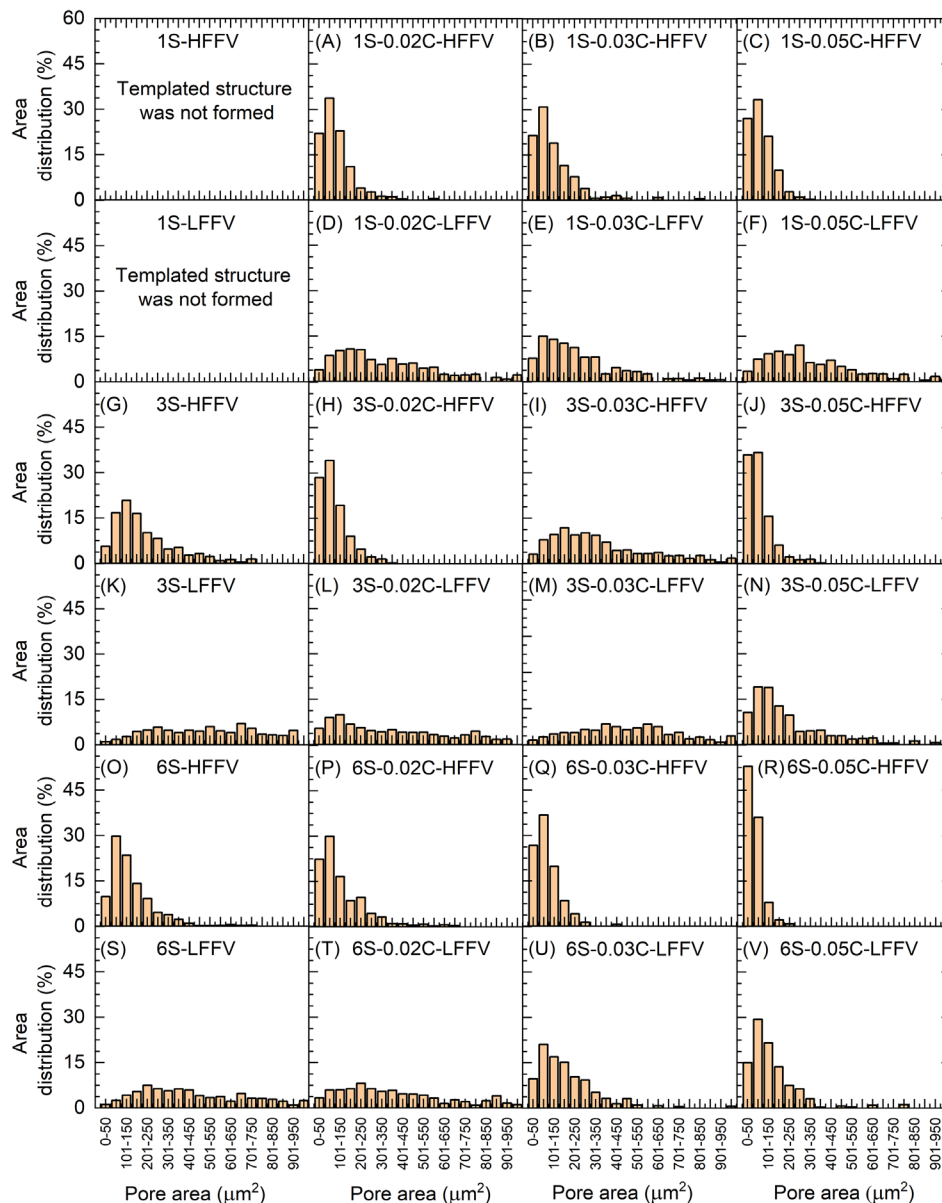
FIGURE 8 Distribution of pore areas estimated from scanning electron microscope (SEM) images of top image plane (5-mm height from bottom) of sintered samples for 1S-0.02C-HFFV (A), 1S-0.02C-LFFV (D), 1S-0.03C-HFFV (B), 1S-0.03C-LFFV (E), 1S-0.05C-HFFV (C), 1S-0.05C-LFFV (F), 3S-HFFV (G), 3S-LFFV (K), 3S-0.02C-HFFV (H), 3S-0.02C-LFFV (L), 3S-0.03C-HFFV (I), 3S-0.03C-LFFV (M), 3S-0.05C-HFFV (J), 3S-0.05C-LFFV (N), 6S-HFFV (O), 6S-LFFV (S), 6S-0.02C-HFFV (P), 6S-0.02C-LFFV (T), 6S-0.03C-HFFV (Q), 6S-0.03C-LFFV (U), 6S-0.05C-HFFV (R), and 6S-0.05C-LFFV (V)

considered was less than 1% of the sample cross-sectional area, and microstructure heterogeneity in LTO materials increased with C_s. Nevertheless, the overall trend was that the population of small pores increased with C_s and FFV.

3.3.5 | Processing–microstructure relationships

Recall that ice-templated microstructure was absent in 1S materials but evolved in the rest of the 1S series. Although

CTAB reduced η, structure formation was not necessarily due to the lowering of η. This was evident because both 3S and 6S materials exhibited well-developed templated microstructure, despite a much higher η than for 1S (Figure 2G). 1S and 6S suspensions had comparable zeta potential as well (Figure 3). Thus, C_s was a driver for ice-templated microstructure formation in 1S series rather than η. As C_s increased, templated microstructure development improved. For 3S series, although η decreased with CTAB and remained comparable despite increasing C_{CT}, the general trend was that dendritic feature increased

with C_s. Similar observations were also made for 6S series.

Increasing η tends to favor the formation of dendritic feature in ice-templated materials.[10,23] However, the current results revealed that dendritic features became prominent even when η decreased. The dependence on C_s was attributed to solid (ice)-liquid (suspension) planar interface instability, which was responsible for the development of ice-templated microstructure.[37] At the initial stage of unidirectional freezing, solid–liquid interface grows as a planar interface. However, solute molecules (dispersant and binder) are rejected by the growth front. As a result, solute concentration increases to C_o/k at the interface but decreases away from the interface to bulk solute concentration C_o. Distribution coefficient k (< 1) describes solute composition difference between liquid and solid phases.[38,39] The exponential decrease of solute concentration in liquid phase (C_l) with distance (x) from interface in the boundary layer is expressed as[38,39]

$$C_l = C_o + (C_o/k - C_o)\exp(-vx/D) \qquad (1)$$

where v is interface velocity and D is solute diffusion coefficient in the liquid. Local equilibrium solidification temperature in the liquid (liquidus temperature, T_{liq}) is reduced at the interface (freezing point depression) but increases away from the interface and reaches bulk T_{liq}, as shown in Figure 9. Actual suspension temperature at any distance from the interface depends on temperature gradient G_L. When G_L is lower than the gradient in T_{liq} curve (indicated by dashed black line), a supercooled region develops ahead of the planar interface where liquid exists below its freezing temperature, which is constitutional supercooling, or more specifically, solute constitutional supercooling effect.[40] ΔT is the maximum degree of supercooling. Metastable constitutionally supercooled liquid provides a driving force for the perturbation of the solid/liquid planar interface, that is, interface instability.[39] Such Mullins–Sekerka (MS)-type instability causes the breakdown of planar interface first to cellular morphology and then into columnar/dendritic morphology.[41] Microstructure evolution in ice-templating thus essentially depends on ΔT.[10,23,37,42]

C_s of 0.02 mol/L in 1S suspensions was insufficient to cause interface instability and thus templated microstructure could not evolve. With CTAB addition, the rest of the 1S series materials exhibited templated microstructure, suggesting that 0.08 mol/L (in 1S-0.02C) was sufficient to cause interface instability. Due to the lack of any composition with C_s between 0.02 and 0.08 mol/L, a more precise threshold C_s for microstructure development was not determined. Microstructure variation with C_s could be attributed to the variation in ΔT, where the higher the
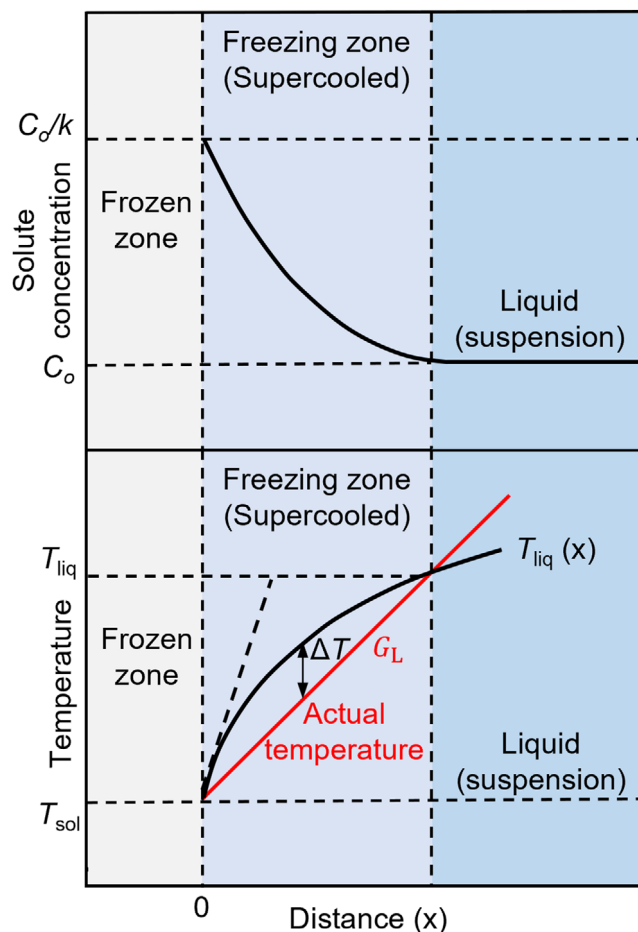

FIGURE 9 Top schematic shows variation in solute concentration and bottom schematic shows variation in liquidus temperature (T_{liq}) with distance (x) from solid–liquid planar interface subject to temperature gradient G_L. Shaded regions shown are frozen zone, freezing zone, and suspension (liquid). The actual suspension temperature in the freezing zone at a distance x from the interface is determined by G_L, whereas T_{liq} (x) represents the equilibrium solidification temperature of the liquid at x. Gradient in T_{liq} curve is indicated by dashed black line.

ΔT the greater the interface instability and microstructure becomes increasingly dendritic.[23] Thus, as C_s increased from 1S to 3S to 6S, ice-templated microstructure evolved and was increasingly dendritic. As η was comparable in these compositions, C_s was likely the driving factor.

For the compositions with comparable C_s but distinctly different microstructures, variations in η needs to be considered. C_s was 0.08 mol/L in 1S-0.02C and 0.09 mol/L in 3S, but microstructure was much finer in 3S than in 1S-0.02C. η was 282 ± 32 mPa·s in 1S-0.02C and 2647 ± 123 mPa·s in 3S. Clearly, η had a role in ice-templated microstructure development between these two materials. As particle entrapment within solvent crystals increases with η, dendritic feature in ice-templated microstructure enhances.[23] However, the role of η can be
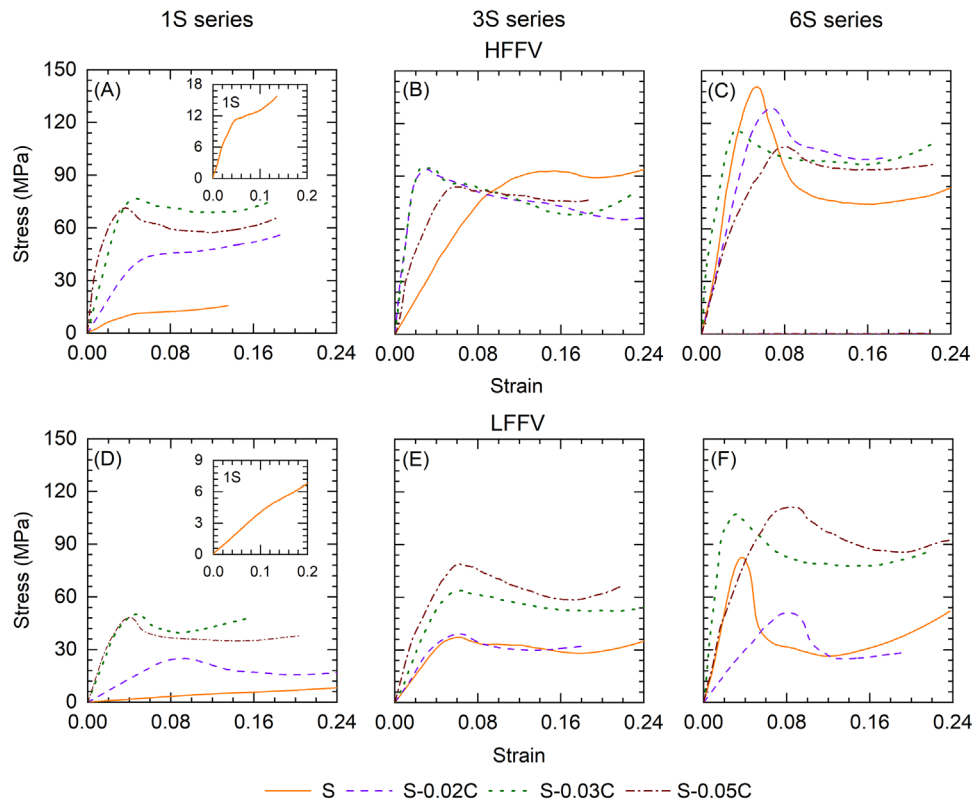
FIGURE 10   Representative uniaxial compressive stress–strain curves for high freezing front velocity (HFFV) (A) 1S series, (B) 3S series, and (C) 6S series lithium titanate oxide (LTO) materials. Similarly, representative uniaxial compressive stress–strain curves for low FFV (LFFV) (D) 1S series, (E) 3S series, and (F) 6S series LTO materials

realized from interface instability as well. The thickness of the boundary layer (δ) ahead of interface can be estimated as[39]

$$\delta = 2D/v. \qquad (2)$$

Thus, δ will decrease with decreasing diffusivity (D) of solute molecules in the suspension. An increase in η decreases D and solute molecules would experience greater resistance to diffuse away from the interface, resulting in a thinner boundary layer. Parai et al.[10] discussed that as the boundary layer becomes thinner, T_{liq} quickly increases away from the interface to reach bulk T_{liq}. Harrison and Tiller[43] reported that steeper solute concentration profiles led to a greater ΔT and driving force for interface instability, which enhanced the fraction of dendritic features. It was interpreted that 3S suspension was at a higher state of metastable condition than 1S-0.02C suspension. As a result, 3S exhibited considerably finer microstructure than 1S-0.02C.

Therefore, for suspensions with comparable η, C_s can be varied to tune ice-templated microstructure, whereas for suspensions with comparable C_s, η variation can tune microstructure. The current study revealed that η and C_s can be separately varied to modify microstructure.

3.4 | Uniaxial compressive mechanical response and structure–property relationships

Figure 10 shows representative uniaxial compressive stress–strain responses of ice-templated LTO materials. All the materials exhibited a linear stress–strain response up to maximum stress where fracture initiated and a stress plateau regime where stress decreased gradually with strain. Although stress in the plateau regime was lower compared to maximum stress, post fracture materials were able to maintain compressive loadbearing capacity. Figure 11 shows the variation of maximum compressive strength with FFV for (A) 1S series, (B) 3S series, and (C) 6S series. The error for compressive strength represents the standard deviation of four independent disks. Figure 11D,E shows variation in strength with C_s in LFFV and HFFV regimes, respectively.

For any composition, strength was consistently higher at HFFV than at LFFV, which was attributed to dendritic morphology in HFFV materials (smaller pores and higher density of bridges between lamella walls) compared to lamellar morphology in LFFV materials (larger pores and lower density of bridges between lamella walls). This trend was consistent with the previous studies that also
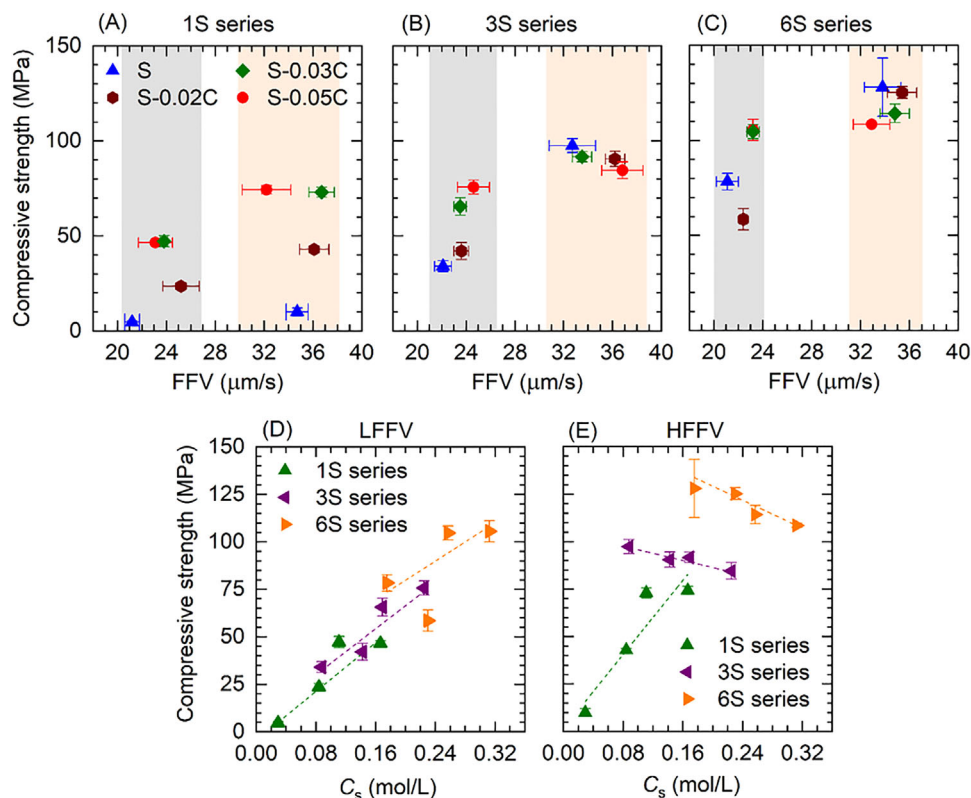
FIGURE 11 Maximum compressive strength at low freezing front velocity (LFFV) and high FFV (HFFV) regimes for (A) 1S series, (B) 3S series, and (C) 6S series materials. Variation in maximum compressive strength with total solute concentration (C_s) for sintered lithium titanate oxide (LTO) materials fabricated at (D) LFFV and (E) HFFV regimes. Error in (A–C) represents the standard deviation for compressive strength of four independent disks.

reported that compressive strength increased with FFV due to the decrease in pore size and increase in bridge density.[9,13–15,20,44–47]

In any series, in LFFV regime, strength increased with C_s. In every series, strength increased significantly up to C_{CT} 0.03 g/cm^3; however, with a further increase in C_{CT}, strength remained about the same or only marginally increased. In the LFFV regime, maximum strength in 1S, 3S, and 6S series was 47.2 ± 3.0, 75.7 ± 3.7, and 105.6 ± 5.6 MPa, respectively. 1S (without templated structure) exhibited the lowest strength, 4.8 ± 0.5 MPa. Thus, as C_s increased from 0.02 (1S) to 0.31 (6S-0.05C) (15-fold increase), strength increased by more than 20-fold.

In the HFFV regime, strength in 1S series also increased with C_s. However, in 3S and 6S series, materials rather exhibited a slight decrease in strength with C_s; thus, 3S and 6S exhibited highest strength in the respective series. In both series, although dendritic feature increased with C_s at HFFV, the resultant structures were probably less efficient for compressive loadbearing. In the HFFV regime, maximum strength in 1S, 3S, and 6S series was 74.4 ± 2.2, 97.5 ± 3.7, and 128.1 ± 15.3 MPa, respectively. 1S (which did not have a templated observed microstructure) exhibited the lowest strength, 10.1 ± 2.1 MPa. Thus, as

C_s increased from 0.02 (1S) to 0.18 (6S) (9-fold increase), strength increased by more than 12-fold.

Therefore, the general trend was that compressive strength increased with C_s. Among the suspensions that only contained sucrose additive, strength increased with C_{su} (1S to 3S to 6S) at both FFV regimes. In these materials, C_{su} was the driving factor for strength increase but not η (Figure 2G). However, a closer look at the strength data also suggested that not only C_s influenced strength but also solute type, where additive type had an influence on η as well. As a result, despite having comparable C_s in several compositions, strength was considerably different. Thus, various factors impacted compressive strength.

For example, C_s was 0.17 mol/L in 1S-0.05C and 3S-0.03C and 0.18 mol/L in 6S, whereas the strength in these materials in LFFV regime was 46.5 ± 1.5, 65.6 ± 4.6, and 78.4 ± 4.4 MPa, respectively. Similar variation in strength among the materials from these compositions also occurred in the HFFV regime, 74.4 ± 2.2, 91.7 ± 2.7, and 128.1 ± 15.3 MPa. Viscosity was 804 ± 9 mPa·s for 1S-0.05C suspension, 399 ± 24 mPa·s for 3S-0.03C suspension, and 2348 ± 202 mPa·s for 6S suspension. Thus, strength increase from 1S-0.05C to 3S-0.03C materials (despite decreasing η) could be due to increased C_{su}.

Similarly, 6S had the highest C_{su} and hence the highest strength. However, as η for 6S was much higher than the other two compositions, it was possible that both C_{su} and η influenced strength.

There were compositions for which strength was comparable but not C_s and η. 1S-0.03C (0.11 mol/L) and 1S-0.05C (0.17 mol/L) materials had comparable strength at both FFV regimes. However, η was 532 ± 19 mPa·s for 1S-0.03C and 804 ± 9 mPa·s for 1S-0.05C. The relative fraction of smaller pores was higher in 1S-0.05C materials than in 1S-0.03C materials, as shown in Figure 8. As microstructure became finer from 1S-0.03C to 1S-0.05C, it would be expected that strength would also increase. However, pore tortuosity likely also increased, which offset the strength increase, and thus strength was comparable.

C_s was comparable in 3S-0.05C (0.22 mol/L) and 6S-0.02C (0.23 mol/L), whereas strength increased (84.5 ± 4.4 to 125.3 ± 3.1 MPa) in the HFFV regime but decreased (75.7 ± 3.7 to 58.5 ± 5.6 MPa) in the LFFV regime. η was 635 ± 32 mPa·s for 3S-0.05C and 322 ± 73 mPa·s for 6S-0.02C. Microstructure was dendritic in the HFFV regime for both materials and the observed strength increase was attributed to increased C_{su}. On the other hand, in the LFFV regime, strength decreased and was attributed to increased wall thickness and pore size.

Therefore, in general, compressive strength increased with C_s. For compositions with comparable C_s, strength increased with C_{su}, where η also increased with C_{su}. Thus, strength was influenced by both C_{su} and η. The current results provide a broad design space for sucrose-based fabrication of ice-templated LTO materials, though it is expected that other metal oxide ceramics with similar pore morphology may exhibit similar behavior. Ice-templated materials were fabricated from 12 different compositions and at two separate FFV regimes with a wide variety of microstructures. As a result, the strength of ice-templated microstructure also varied over a wide range, 23.6–128.1 MPa, whereas all the sintered porous materials had comparable pore/void fractions. Microstructure and strength tuning factors were FFV, C_s, C_{su}, and η. Use of two additives in different proportions allowed a systematic alteration of C_s and η. The current results revealed that the compressive strength of ice-templated materials can increase even when η decreases. η decreased due to cationic dispersant; however, increase in C_s enhanced dendritic feature in microstructure and hence strength.

In summarizing, highest compressive strength was achieved in 6S series materials that were fabricated in the HFFV regime. Thus, high C_s and FFV were the most suitable processing parameters to achieve highest compressive strength in ice-templated LTO materials that were fabricated, without changing total porosity. The microstructural origin for highest strength in 6S series materials was attributed to the observed highly dendritic morphology resulting from finer pores and higher density of lamellar bridges compared to the other series materials. In 6S series materials, particularly which were fabricated in the HFFV regime, a prominent microstructural feature was that almost uniform dendritic morphology was maintained over the compression test specimen thickness (3 mm) in the growth direction of ice crystals. This was opposed to the other series materials where over the same distance, morphology was observed to be dendritic in the bottom region of the test specimens but turned lamellar by the top region. For ice-templated ceramic materials, it has been shown that strength decreases as morphology changes from dendritic to lamellar.[9,13–15,20,44,45,47] Therefore, the current results revealed that the role of high C_s and FFV was to preserve highly dendritic morphology throughout the ice-templated microstructure in the growth direction of ice crystals, which was beneficial to achieve markedly high compressive strength.

4 | CONCLUSIONS

All aqueous suspensions contained 27-vol.% LTO particles. However, the concentration of sucrose and cationic dispersant CTAB was systematically varied, and ice-templating was performed at two distinctly FFV regimes. Selected sucrose concentrations (C_{su}) were 1, 3, and 6 wt.% (weight of sucrose with respect to DI water content in suspension). Selected CTAB concentrations (C_{CT}) were 0.02, 0.03, and 0.05 g/cm^3 (weight of dispersant with respect to DI water volume in suspension). With respect to DI water content, 0.02, 0.03, and 0.05g/cm^3 CTAB corresponded to 2, 3, and 5wt.% CTAB. Materials were fabricated between 32–36 (HFFV regime) and 21–25 μm/s (LFFV regime). Based on the results, the following conclusions were made:

1. Although CTAB decreased the viscosity of aqueous LTO suspensions to a greater extent than sucrose, a combination of them was more effective in reducing viscosity. Based on the viscosity and zeta potential results, 12 suspension compositions were developed, and 96 ice-templated LTO samples were fabricated.

2. All ice-templated sintered materials were of comparable porosity (between 47 and 52 vol.%), irrespective of suspension composition, viscosity, and FFV.

3. Total solute concentration (C_s, mol/L) and FFV had a pronounced impact on ice-templated microstructure. Development of ice-templated microstructure was dependent on total solute concentration and microstructure development improved with solute concentration. Morphology was dendritic

in the HFFV regime but lamellar in the LFFV regime. Dendritic feature increased with solute concentration. However, comparable solute concentration did not necessarily result in similar microstructure.

4. Microstructure dependence on solute concentration was rationalized based on MS-type interface instability and the degree of supercooling. The results revealed that for suspensions with comparable viscosity, solute concentration can be varied to tune microstructure, whereas for suspensions with comparable solute concentration, viscosity variation can tune microstructure.

5. Compressive strength increased with solute concentration and FFV. For comparable total solute concentration, strength increased with both sucrose concentration and viscosity.

6. High solute concentration and FFV were the most suitable processing parameters to achieve highest compressive strength in ice-templated LTO materials, where the role of these parameters was to preserve highly dendritic morphology throughout the ice-templated microstructure in the growth direction of ice crystals.

7. The current study thus provides a broad design space for the sucrose-based fabrication of ice-templated LTO materials. Using 12 different suspension compositions, a wide variety of microstructures was developed. As a result, strength also varied over a wide range, 23.6–128.1 MPa.

ORCID

Dipankar Ghosh https://orcid.org/0000-0002-4574-9600

REFERENCES

1. Huang C, Grant PS. Coral-like directional porosity lithium-ion battery cathodes by ice templating. J Mater Chem A. 2018;6:14689–99.

2. Delattre B, Amin R, Sander J, Coninck JD, Tomsia AP, Chiang YM. Impact of pore tortuosity on electrode kinetics in lithium battery electrodes: study in directionally freeze-cast $LiNi_{0.8}Co_{0.15}Al_{0.05}O_2$(NCA). J Electrochem Soc. 2018;165(2):A388–95.

3. Huang C, Dontigny M, Zaghib K, Grant PS. Low-tortuosity and graded lithium ion battery cathodes by ice templating, J Mater Chem A. 2019;7(37):21421–31.

4. Du G, Zhou Y, Tian X, Wu G, Xi Y, Zhao S. High-performance 3D directional porous $LiFePO_4$/C materials synthesized by freeze casting. Appl Surf Sci. 2018;453:493–501.

5. Deville S. Ice-templating, freeze casting: beyond materials processing. J Mater Res. 2013;28(17):2202–19.

6. Zavareh S, Hilger A, Hirselandt K, Goerke O, Manke I, Banhart J, Gurlo A. Fabrication of cellular and lamellar $LiFePO_4$/C cathodes for Li-ion batteries by unidirectional freeze casting method. J Ceram Soc Jpn. 2016;124(10):1067–71.

7. Nie Z, Parai R, Cai C, Michaelis C, LaManna JM, Hussey DS, et al. Pore microstructure impacts on lithium-ion transport and rate capability of thick sintered electrodes. J Electrochem Soc. 2021;168(6):060550.

8. Nie Z, Parai R, Chen C, Ghosh D, Koenig Jr GM. Improving high rate cycling limitations of thick sintered battery electrodes by mitigating molecular transport limitations through modifying electrode microstructure and electrolyte conductivity. Mol Syst Des Eng. 2021;6(9):708–12.

9. Parai R, Walters T, Marin J, Pagola S, Koenig Jr GM, Ghosh D. Strength enhancement in ice-templated lithium titanate $Li_4Ti_5O_{12}$ materials using sucrose. Materialia. 2020;14:100901.

10. Parai R, Gundrati NB, Akurati S, Koenig Jr GM, Ghosh D. Microstructure in the transition region and steady-state region of ice-templated sintered lithium titanate $Li_4Ti_5O_{12}$ materials fabricated with and without sucrose. J Mater Res. 2021;36(17):3519–38.

11. Kim H. Effects of mechanical stresses on lithium-ion batteries. PhD dissertation. Ann Arbor, MI: University of Michigan; 2009.

12. Pender JP, Jha G, Youn DH, Ziegler JM, Andoni I, Choi EJ, et al. Electrode degradation in lithium-ion batteries. J Am Chem Soc. 2020;12(2):1243–95.

13. Akurati S, Ghosh D, Banda M, Terrones DA. Direct observation of failure in ice templated ceramics under dynamic and quasistatic compressive loading conditions. J Dyn Behav Mater. 2019;5(4):463–83.

14. Ghosh D, Dhavale N, Banda M, Kang H. A comparison of microstructure and uniaxial compressive response of ice-templated alumina scaffolds fabricated from two different particle sizes. Ceram Int. 2016;42(14):16138–47.

15. Ghosh D, Kang H, Banda M, Kamaha V. Influence of anisotropic grains (platelets) on the microstructure and uniaxial compressive response of ice-templated sintered alumina scaffolds. Acta Mater. 2017;125:1–14.

16. Munch E, Saiz E, Tomsia AP, Deville S. Architectural control of freeze-cast ceramics through additives and templating. J Am Ceram Soc. 2009;92(7):1534–39.

17. Frank MB, Siu SH, Karandikar K, Liu CH, Naleway SE, Porter MM, et al. Synergistic structures from magnetic freeze casting with surface magnetized alumina particles and platelets. J Mech Behav Biomed Mater. 2017;76:153–63.

18. Ogden TA, Prisbrey M, Nelson I, Raeymaekers B, Naleway SE. Ultrasound freeze casting: fabricating bioinspired porous scaffolds through combining freeze casting and ultrasound directed self-assembly. Mater Des. 2019;164:107561.

19. Tang Y, Qiu S, Miao Q, Wu C. Fabrication of lamellar porous alumina with axisymmetric structure by directional solidification with applied electric and magnetic fields. J Eur Ceram Soc. 2016;36(5):1233–40.

20. Akurati S, Qian S, Ghosh D. AC electric field-assisted fabrication of ice-templated alumina materials and remarkable enhancement of compressive strength. Scr Mater. 2022;206:114264.

21. Zhang Y, Hu L, Han J, Jiang Z. Freeze casting of aqueous alumina slurries with glycerol for porous ceramics. Ceram Int. 2010;36(2):617–21.

22. Tang Y, Qiu S, Wu C, Miao Q, Zhao K. Freeze cast fabrication of porous ceramics using tert-butyl alcohol–water crystals as template. J Eur Ceram Soc. 2016;36(6):1513–8.

23. Porter MM, Imperio R, Wen M, Meyers MA, McKittrick J. Bioinspired scaffolds with varying pore architectures and mechanical properties. Adv Funct Mater. 2014;24(14):1978–87.

24. Zeng J, Zhang Y, Zhou K-C, Zhang D. Effects of alcohol additives on pore structure and morphology of freeze-cast ceramics. Trans Nonferrous Met Soc China. 2014;24(3):718–22.

25. Zou J, Zhang Y, Li R. Effect of suspension state on the pore structure of freeze-cast ceramics. Int J Appl Ceram Technol. 2011;8(2):482–9.

26. White MA, Conrad J, Ellis SN, Chen R. Investigations of ice-structuring agents in ice-templated ceramics. J Am Ceram Soc. 2017;100(11):5066–74.

27. Pekor C, Groth B, Nettleship I. The effect of polyvinyl alcohol on the microstructure and permeability of freeze-cast alumina. J Am Ceram Soc. 2010;93(1):115–20.

28. Zuo KH, Zeng YP, Jiang D. Properties of microstructure-controllable porous yttria-stabilized zirconia ceramics fabricated by freeze casting. Int J Appl Ceram Technol. 2008;5(2):198–203.

29. Antaris D, Dillon S, Chasiotis I. Effect of porosity on electrochemical and mechanical properties of composite Li-ion anodes. J Compos Mater. 2015;49(15):1849–62.

30. Dhavale ND. A comparison of microstructure and uniaxial compressive response of ice-templated porous alumina scaffolds fabricated from two different particle sizes. Master's thesis. Norfolk, VA: Old Dominion University; 2016.

31. Qi Z, Koenig Jr GM. A carbon-free lithium-ion solid dispersion redox couple with low viscosity for redox flow batteries. J Power Sources. 2016;323:97–106.

32. Kim JC, Schilling CH, Tomasik P, Auh KH. Plasticizing dense alumina slurries with mono- and di-saccharides. Matter Lett. 2000;42(4):221–4.

33. Wang X, Guo L. Effect of sucrose on rheological properties of aqueous zirconia suspensions with polyacrylate. Powder Technol. 2008;186(2):107–12.

34. Pradhan M, Bhargava P. Effect of sucrose on fabrication of ceramic foams from aqueous slurries. J Am Ceram Soc. 2005;88(1):216–8.

35. Felicia LJ, Johnson JC, Phillip J. Effect of surfactant on the size, zeta potential and rheology of alumina nanofluids. J Nanofluids. 2014;3(4):328–35.

36. Li C, Akinc M. Role of bound water on the viscosity of nanometric alumina suspensions, J Am Ceram Soc. 2005;88(6):1448–54.

37. Deville S, Maire E, Lasalle A, Bogner A, Gauthier C, Leloup J, et al. In situ X-ray radiography and tomography observations of the solidification of aqueous alumina particle suspensions—Part I: Initial instants. J Am Ceram Soc. 2009;92:2489–96.

38. Glicksman ME. Principles of solidification. New York: Springer; 2011.

39. Pekor CM. The effect of water-soluble polymers on the microstructure and properties of freeze-cast alumina ceramics. PhD Dissertation. University of Pittsburgh; 2010.

40. You J, Wang L, Wang Z, Li J, Wang J, Lin X, Huang W. Inter-facial undercooling in solidification of colloidal suspensions: analyses with quantitative measurements. Sci Rep. 2016;6(1):1–7.

41. Mullins WW, Sekerka RF. Stability of a planar interface during solidification of dilute binary alloy. J App Phys. 1964;35(2):444–51.

42. Deville S, Saiz E, Tomsia AP. Ice-templated porous alumina structures. Acta Mater. 2007;55(6):1965–74.

43. Harrison JD, Tiller WA. Ice interface morphology and texture developed during freezing. J Appl Phys. 1963;34(11):3349–55.

44. Banda M, Akurati S, Ghosh D. Governing role of the ratio of large platelet particles to ultrafine particles on dynamic and quasistatic compressive response and damage evolution in ice-templated alumina ceramics. J Mater Res. 2020;35(21):2870–86.

45. Banda M, Ghosh D. Effects of temperature and platelets on lamella wall microstructure, structural stability, and compressive strength in ice-templated ceramics. Materialia. 2020;9:100537(1-16).

46. Akurati S, Marin J, Gundrati B, Ghosh D. Assessing the role of loading direction on the uniaxial compressive response of multilayered ice-templated alumina-epoxy composites. Materialia. 2020;14:100895(1-15).

47. Ghosh D, Banda M, Dhavale N, Kang H. Platelet-induced stiffening and strengthening of ice-templated Al_2O_3 scaffolds. Scr Mater. 2016;125:29–33.